

Computational Performance of a LES Solver for Supersonic Jet Flow Applications

Carlos Junqueira-Junior* and João Luiz F. Azevedo†

Instituto de Aeronáutica e Espaço, 12228-904 São José dos Campos, SP, Brazil

Sami Yamouni‡

Instituto Tecnológico de Aeronáutica, 12228-900 São José dos Campos, SP, Brazil

William R. Wolf §

Universidade Estadual de Campinas, 13083-970 Campinas, SP, Brazil

Abstract

An in-house large eddy simulation tool is developed in order to reproduce high fidelity results of compressible jet flows. The large eddy simulation formulation is written using the finite difference approach, with an explicit time integration and using a second order spatial discretization. The energy equation is carefully discretized in order to model the energy equation of the filtered Navier-Stokes formulation. Such numerical studies are very expensive and demand high performance computing. Message passage interface protocols are implemented into the code in order to perform parallel computations. The present work addresses the computational performance of the solver running on up to 400 processors in parallel. Different mesh configurations, whose size varies from approximately 5.9 million points to approximately 1.0 billion points, are evaluate in the current paper. Speedup and efficiency curves are evaluated in order to assess the strong scalability of the solver.

I. Introduction

Solid structure of different parts of launch vehicles and experimental apparatus on board can be damaged during the take off and also during the transonic flight of such vehicles due to vibrational acoustic stress resulted from pressure fluctuations. Such fluctuations are originated from the complex interaction between the high-temperature/high-velocity exhaust gases from the rocket engines. The acoustic design constraints of launch vehicles have encouraged the studies of aeroacoustic fields around compressible jet flows for aerospace applications. Instituto de Aeronautica e Espaço (IAE) has been using large eddy simulations (LES)^{1,2} coupled with the Ffowcs Williams and Hawkings approach³ in order to study the aeroacoustic of supersonic jet flow configurations. The LES studies are very expensive in the computational context and strongly demand parallel computing. The present work addresses the computational performance of the solver using up to 400 processors in parallel. The speedup and computational efficiency of the solver are measured using different mesh and partition configurations and different number of computational cores.

*Postdoctoral Research Fellow, Aerodynamics Division, Departamento de Ciência e Tecnologia Aeroespacial, DCTA/IAE/ALA; E-mail: junior.hmg@gmail.com.

†Senior Research Engineer, Aerodynamics Division, Departamento de Ciência e Tecnologia Aeroespacial, DCTA/IAE/ALA; E-mail: joaoluiz.azevedo@gmail.com. AIAA Fellow.

‡Postdoctoral Reasearch Fellow, Graduate Program on Computer Sciences and Electrical Engineering, Departamento de Ciência e Tecnologia Aeroespacial, DCTA/ITA; E-mail: sami.yamouni@gmail.com.

§Assistant Professor, Faculty of Mechanical Engineering; E-mail: wolf@fem.unicamp.br. AIAA Member

JAZzY¹ is the LES solver which is used in the present work. It is an in-house computational tool developed regarding the study of unsteady turbulent supersonic jet flow configurations. The formulation is written using the finite difference approach. Inviscid numerical fluxes are calculated using a second order accurate centered scheme with the explicit addition of artificial dissipation. A five steps second order accurate Runge-Kutta is the chosen time marching method. A formulation based on the System I set of equations⁴ is used here in order to model the filtered terms of the energy equation. Numerical simulation of perfectly expanded jets are performed and compared with numerical⁵ and experimental⁶ data.

The code is written using the FORTRAN 90 standards. It uses the *HDF5*^{7,8} and the *CGNS*^{9–11} libraries for the I/O operations. The mesh is partitioned into the axial and azimuthal directions. Two layer ghost points are created at the surroundings of the local domain in order to carry neighbor partitions data. The data exchange between partitions is performed through message passing interface (MPI) protocols.¹²

Simulations of a perfectly expanded jet are performed using different mesh partitioning and different number of processors in order to evaluate the computational performance of the code. In the present nine meshes are studied running on up to 400 processors in parallel. The size of the mesh starts with 5.8 million points and scales to 1.0 billion points. The speedup and computational efficiency curves are presented and compared in order to study the strong scalability of the code.

II. Large Eddy Simulation Filtering

The large eddy simulation is based on the principle of scale separation, which is addressed as a filtering procedure in a mathematical formalism. A modified version of the the System I filtering approach⁴ is used in present work which is given by

$$\begin{aligned} \frac{\partial \bar{p}}{\partial t} + \frac{\partial}{\partial x_j} (\bar{\rho} \tilde{u}_j) &= 0, \\ \frac{\partial}{\partial t} (\bar{\rho} \tilde{u}_i) + \frac{\partial}{\partial x_j} (\bar{\rho} \tilde{u}_i \tilde{u}_j) + \frac{\partial \bar{p}}{\partial x_i} - \frac{\partial \tau_{ij}}{\partial x_j} + \frac{1}{3} \frac{\partial}{\partial x_j} (\delta_{ij} \sigma_{ii}) &= 0, \\ \frac{\partial \bar{e}}{\partial t} + \frac{\partial}{\partial x_j} [(\bar{e} + \bar{p}) \tilde{u}_j] - \frac{\partial}{\partial x_j} (\tau_{ij} \tilde{u}_i) + \frac{1}{3} \frac{\partial}{\partial x_j} [(\delta_{ij} \sigma_{ii}) \tilde{u}_i] + \frac{\partial q_j}{\partial x_j} &= 0, \end{aligned} \quad (1)$$

in which t and x_i are independent variables representing time and spatial coordinates of a Cartesian coordinate system \mathbf{x} , respectively. The components of the velocity vector \mathbf{u} are written as u_i , and $i = 1, 2, 3$. Density, pressure and total energy per mass unit are denoted by ρ , p and e , respectively. The $(\bar{\cdot})$ and $(\tilde{\cdot})$ operators are used in order to represent filtered and Favre averaged properties, respectively. The System I formulation neglects the double correlation term and the total energy per mass unit is written as

$$\bar{e} = \frac{\bar{p}}{\gamma - 1} + \frac{1}{2} \rho \tilde{u}_i \tilde{u}_i. \quad (2)$$

The heat flux, q_j , is given by

$$q_j = (\kappa + \kappa_{sgs}) \frac{\partial \tilde{T}}{\partial x_j}. \quad (3)$$

where T is the static temperature and κ is the thermal conductivity, which can be expressed by

$$\kappa = \frac{\mu C_p}{Pr}, \quad (4)$$

The thermal conductivity is a function of the specific heat at constant pressure, C_p , of the Prandtl number, Pr , which is equal to 0.72 for air, and of the dynamic viscosity, μ . The SGS thermal conductivity, κ_{sgs} , is written as

$$\kappa_{sgs} = \frac{\mu_{sgs} C_p}{Pr_{sgs}}, \quad (5)$$

where Pr_{sgs} is the SGS Prandtl number, which is equal to 0.9 for static SGS models and μ_{sgs} is the eddy viscosity which is calculated by the SGS closure. The dynamic viscosity, μ , can be calculated using the Sutherland law,

$$\mu(\tilde{T}) = \mu_\infty \left(\frac{\tilde{T}}{\tilde{T}_\infty} \right)^{\frac{3}{2}} \frac{\tilde{T}_0 + S_1}{\tilde{T} + S_1} \quad \text{with } S_1 = 110.4K. \quad (6)$$

Density, static pressure and static temperature are correlated by the equation of state given by

$$\bar{p} = \rho R \tilde{T}, \quad (7)$$

where R is the gas constant, written as

$$R = C_p - C_v, \quad (8)$$

and C_v is the specific heat at constant volume. The shear-stress tensor, τ_{ij} , is written according to the Stokes hypothesis and includes the eddy viscosity, μ_{sgs} ,

$$\tau_{ij} = 2(\mu + \mu_{sgs}) \left(\tilde{S}_{ij} - \frac{1}{3} \delta_{ij} \tilde{S}_{kk} \right) \quad (9)$$

in which \tilde{S}_{ij} , components of rate-of-strain tensor, are given by

$$\tilde{S}_{ij} = \frac{1}{2} \left(\frac{\partial \tilde{u}_i}{\partial x_j} + \frac{\partial \tilde{u}_j}{\partial x_i} \right). \quad (10)$$

The SGS stress tensor components are written using the eddy viscosity,¹³

$$\sigma_{ij} = -2\mu_{sgs} \left(\tilde{S}_{ij} - \frac{1}{3} \tilde{S}_{kk} \right) + \frac{1}{3} \delta_{ij} \sigma_{kk}. \quad (11)$$

The eddy viscosity, μ_{sgs} , and the components of the isotropic part of the SGS stress tensor, σ_{kk} , are modeled by the SGS closure.

III. Subgrid Scale Modeling

The theoretical formulation of subgrid scales closures included in the present work is discussed in the present section. The closure models presented here are founded on the homogeneous turbulence theory, which is usually developed in the spectral space as an attempt to quantify the interaction between the different scales of turbulence.

III.A. Smagorinsky Model

The Smagorinsky model¹⁴ is one of the simplest algebraic models for the deviatoric part of the SGS tensor used in large-eddy simulations. The isotropic part of the SGS tensor is neglected for Smagorinsky model in the current work. This SGS closure is a classical model based the large scales properties and is written as

$$\mu_{sgs} = (\rho C_s \Delta)^2 |\tilde{S}|, \quad (12)$$

where

$$|\tilde{S}| = \left(2\tilde{S}_{ij}\tilde{S}_{ij} \right)^{\frac{1}{2}}, \quad (13)$$

Δ is the filter size and C_s is the Smagorinsky constant. Several attempts can be found in the literature regarding the evaluation of the Smagorinsky constant. The value of this constant is adjusted to improve the results of different flow configurations. In practical terms, the Smagorinsky subgrid model has a flow dependency of the constant which takes value ranging from 0.1 to 0.2 depending on the flow. The suggestion of Lilly,¹⁵ $C_s = 0.148$, is used in the current work.

This model is generally over-dissipative in regions of large mean strain. This is particularly true in the transitional region between laminar and turbulent flows. Moreover, the limiting behavior near the wall is not correct, and the model predictions correlate poorly with the exact subgrid scale tensor.¹⁶ However, it is a very simple model and, with the use of damping function and good calibration, can be successfully applied on large-eddy simulations.

III.B. Vreman Model

Vreman¹⁷ proposed a turbulence model that can correctly predict inhomogeneous turbulent flows. For such flows, the eddy viscosity should become small in laminar and transitional regions. This requirement is unfortunately not satisfied by existing simple eddy-viscosity closures such as the classic Smagorinsky model.^{14, 18, 19} The Vreman SGS model is very simple and is given by

$$\mu_{sgs} = \rho \mathbf{c} \sqrt{\frac{B_\beta}{\alpha_{ij}\alpha_{ij}}}, \quad (14)$$

with

$$\alpha_{ij} = \frac{\partial \tilde{u}_j}{\partial x_i}, \quad (15)$$

$$\beta_{ij} = \Delta_m^2 \alpha_{mi} \alpha_{mj} \quad (16)$$

and

$$B_\beta = \beta_{11}\beta_{22} - \beta_{12}^2 + \beta_{11}\beta_{33} - \beta_{13}^2 + \beta_{22}\beta_{33} - \beta_{23}^2. \quad (17)$$

The constant \mathbf{c} is related to the Smagorinsky constant, C_s , and it is given by

$$\mathbf{c} = 2.5 C_s^2, \quad (18)$$

and Δ_m is the filter width in each direction. In the present work, the isotropic part of the SGS tensor is neglected for the Vreman model. The α symbol represents the matrix of first order derivatives of the filtered components of velocity, \tilde{u}_i . The SGS eddy-viscosity is defined as zero when $\alpha_{ij}\alpha_{ij}$ equals zero. Vreman¹⁷ affirms that the tensor β is proportional to the gradient model^{20, 21} in its general anisotropic form.²²

The Vreman model can be classified as very simple model because it is expressed in first-order derivatives and it does not involve explicit filtering, averaging, clipping procedures and is rotationally invariant for isotropic filter widths. The model is originally created for incompressible flows and it has presented good results for two incompressible flows configurations: the transitional and turbulent mixing layer at high Reynolds number and the turbulent channel flow.²² In both cases, the Vreman model is found to be more accurate than the classical Smagorinsky model and as good as the dynamic Smagorinsky model.

III.C. Dynamic Smagorinsky Model

Germano *et al.*²³ developed a dynamic SGS model in order to overcome the issues of the classical Smagorinsky closure. The model uses the strain rate fields at two different scales and thus extracts spectral information in the large-scale field to extrapolate the small stresses.²⁴ The coefficients of the model are computed instantaneously in the dynamic model. They are function of the positioning in space and time rather than being specified a priori. Moin *et al.*²⁴ extended the work of Germano for compressible flows. The dynamic Smagorinsky model for compressible flow configurations is detailed in the present section.

The Dynamic model introduces the test filter, $\widehat{(\cdot)}$, which has a larger filter width, $\widehat{\Delta}$, than the one of the resolved grid filter, $\overline{(\cdot)}$. The use of test filters generates a second field with larger scales than the resolved field. The Yoshizawa model²⁵ is used for the isotropic portion of the SGS tensor and it is written as

$$\sigma_{ii} = 2C_I \bar{\rho} \Delta^2 |\tilde{S}|^2, \quad (19)$$

where C_I is defined by

$$C_I = \frac{\left\langle \widehat{\bar{\rho} \tilde{u}_i \tilde{u}_i} - \left(\widehat{\bar{\rho} \tilde{u}_i} \widehat{\bar{\rho} \tilde{u}_i} / \widehat{\bar{\rho}} \right) \right\rangle}{\left\langle 2\widehat{\Delta}^2 \widehat{\bar{\rho}} |\widehat{S}|^2 - 2\Delta^2 \bar{\rho} |\tilde{S}|^2 \right\rangle}. \quad (20)$$

A volume averaging, here indicated by $\langle \cdot \rangle$, is suggested by Moin *et al.*²⁴ and by Garnier *et al.* in order to avoid numerical issues. The eddy viscosity, μ_{sgs} , is calculated using the same approach used by static Smagorinsky model,

$$\mu_{sgs} = (\rho C_{ds} \Delta)^2 |\tilde{S}|, \quad (21)$$

where

$$|\tilde{S}| = \left(2\tilde{S}_{ij}\tilde{S}_{ij}\right)^{\frac{1}{2}}, \quad (22)$$

and C_{ds} is the dynamic constant of the model, which is given by

$$C_{ds} = \frac{\left\langle \left[\widehat{\overline{\rho\tilde{u}_i\tilde{u}_j}} - \left(\widehat{\overline{\rho\tilde{u}_i}}\widehat{\overline{\rho\tilde{u}_j}}/\widehat{\overline{\rho}} \right) \right] \tilde{S}_{ij} - \frac{1}{3}\tilde{S}_{mm}(\mathcal{T}_{ll} - \hat{\sigma}_{ll}) \right\rangle}{\left\langle 2\Delta^2 \left[\widehat{\overline{\rho|\tilde{S}|}}\tilde{S}_{ij}\tilde{S}_{ij} - \frac{1}{3}\left(\widehat{\overline{\rho|\tilde{S}|}}\tilde{S}_{mm}\right)\widehat{\overline{\rho|\tilde{S}|}}\right] - 2\hat{\Delta}^2 \left(\widehat{\overline{\rho|\tilde{S}|}}\widehat{\overline{\rho|\tilde{S}|}}\tilde{S}_{ij}\tilde{S}_{ij} - \frac{1}{3}\widehat{\overline{\rho|\tilde{S}|}}\widehat{\overline{\rho|\tilde{S}|}}\tilde{S}_{mm}\tilde{S}_{ll} \right) \right\rangle}. \quad (23)$$

The SGS Prandtl number is computed using the dynamic constant, C_{ds} , and written as

$$Pr_{sgs} = C_{ds} \frac{\left\langle \Delta^2 \left(\widehat{\overline{\rho|\tilde{S}|}} \frac{\partial \tilde{T}}{\partial x_j} \right) \frac{\partial \tilde{T}}{\partial x_j} - \hat{\Delta}^2 \widehat{\overline{\rho|\tilde{S}|}} \frac{\partial \tilde{T}}{\partial x_j} \frac{\partial \tilde{T}}{\partial x_j} \right\rangle}{\left\langle \left[\widehat{\overline{\rho\tilde{u}_j\tilde{T}}} - \left(\widehat{\overline{\rho\tilde{u}_j}}\widehat{\overline{\rho\tilde{T}}} \right) / \widehat{\overline{\rho}} \right] \frac{\partial \tilde{T}}{\partial x_j} \right\rangle}. \quad (24)$$

IV. Transformation of Coordinates

The formulation is written in the a general curvilinear coordinate system in order to facilitate the implementation and add more generality for the CFD tool. Hence, the filtered Navier-Stokes equations can be written in strong conservation form for a 3-D general curvilinear coordinate system as

$$\frac{\partial \hat{Q}}{\partial t} + \frac{\partial}{\partial \xi} \left(\hat{\mathbf{E}}_e - \hat{\mathbf{E}}_v \right) + \frac{\partial}{\partial \eta} \left(\hat{\mathbf{F}}_e - \hat{\mathbf{F}}_v \right) + \frac{\partial}{\partial \zeta} \left(\hat{\mathbf{G}}_e - \hat{\mathbf{G}}_v \right) = 0. \quad (25)$$

In the present work, the chosen general coordinate transformation is given by

$$\begin{aligned} \xi &= \xi(x, y, z, t), \\ \eta &= \eta(x, y, z, t), \\ \zeta &= \zeta(x, y, z, t). \end{aligned} \quad (26)$$

In the jet flow configuration, ξ is the axial jet flow direction, η is the radial direction and ζ is the azimuthal direction. The vector of conserved properties is written as

$$\hat{Q} = J^{-1} [\bar{\rho} \quad \bar{\rho}\tilde{u} \quad \bar{\rho}\tilde{v} \quad \bar{\rho}\tilde{w} \quad \bar{e}]^T, \quad (27)$$

where the Jacobian of the transformation, J , is given by

$$J = (x_\xi y_\eta z_\zeta + x_\eta y_\zeta z_\xi + x_\zeta y_\xi z_\eta - x_\xi y_\zeta z_\eta - x_\eta y_\xi z_\zeta - x_\zeta y_\eta z_\xi)^{-1}, \quad (28)$$

and

$$\begin{aligned} x_\xi &= \frac{\partial x}{\partial \xi}, & x_\eta &= \frac{\partial x}{\partial \eta}, & x_\zeta &= \frac{\partial x}{\partial \zeta}, \\ y_\xi &= \frac{\partial y}{\partial \xi}, & y_\eta &= \frac{\partial y}{\partial \eta}, & y_\zeta &= \frac{\partial y}{\partial \zeta}, \\ z_\xi &= \frac{\partial z}{\partial \xi}, & z_\eta &= \frac{\partial z}{\partial \eta}, & z_\zeta &= \frac{\partial z}{\partial \zeta}. \end{aligned} \quad (29)$$

The inviscid flux vectors, $\hat{\mathbf{E}}_e$, $\hat{\mathbf{F}}_e$ and $\hat{\mathbf{G}}_e$, are given by

$$\hat{\mathbf{E}}_e = J^{-1} \begin{Bmatrix} \bar{\rho}U \\ \bar{\rho}\tilde{u}U + \bar{p}\xi_x \\ \bar{\rho}\tilde{v}U + \bar{p}\xi_y \\ \bar{\rho}\tilde{w}U + \bar{p}\xi_z \\ (\bar{e} + \bar{p})U - \bar{p}\xi_t \end{Bmatrix}, \quad \hat{\mathbf{F}}_e = J^{-1} \begin{Bmatrix} \bar{\rho}V \\ \bar{\rho}\tilde{u}V + \bar{p}\eta_x \\ \bar{\rho}\tilde{v}V + \bar{p}\eta_y \\ \bar{\rho}\tilde{w}V + \bar{p}\eta_z \\ (\bar{e} + \bar{p})V - \bar{p}\eta_t \end{Bmatrix}, \quad \hat{\mathbf{G}}_e = J^{-1} \begin{Bmatrix} \bar{\rho}W \\ \bar{\rho}\tilde{u}W + \bar{p}\zeta_x \\ \bar{\rho}\tilde{v}W + \bar{p}\zeta_y \\ \bar{\rho}\tilde{w}W + \bar{p}\zeta_z \\ (\bar{e} + \bar{p})W - \bar{p}\zeta_t \end{Bmatrix}. \quad (30)$$

The contravariant velocity components, U , V and W , are calculated as

$$\begin{aligned} U &= \xi_x \bar{u} + \xi_y \bar{v} + \xi_z \bar{w}, \\ V &= \eta_x \bar{u} + \eta_y \bar{v} + \eta_z \bar{w}, \\ W &= \zeta_x \bar{u} + \zeta_y \bar{v} + \zeta_z \bar{w}. \end{aligned} \quad (31)$$

The metric terms are given by

$$\begin{aligned} \xi_x &= J(y_\eta z_\zeta - y_\zeta z_\eta), & \xi_y &= J(z_\eta x_\zeta - z_\zeta x_\eta), & \xi_z &= J(x_\eta y_\zeta - x_\zeta y_\eta), \\ \eta_x &= J(y_\eta z_\xi - y_\xi z_\eta), & \eta_y &= J(z_\eta x_\xi - z_\xi x_\eta), & \eta_z &= J(x_\eta y_\xi - x_\xi y_\eta), \\ \zeta_x &= J(y_\xi z_\eta - y_\eta z_\xi), & \zeta_y &= J(z_\xi x_\eta - z_\eta x_\xi), & \zeta_z &= J(x_\xi y_\eta - x_\eta y_\xi). \end{aligned} \quad (32)$$

$$(33)$$

The viscous flux vectors, $\hat{\mathbf{E}}_v$, $\hat{\mathbf{F}}_v$ and $\hat{\mathbf{G}}_v$, are written as

$$\hat{\mathbf{E}}_v = J^{-1} \begin{pmatrix} 0 \\ \xi_x \tau_{xx} + \xi_y \tau_{xy} + \xi_z \tau_{xz} \\ \xi_x \tau_{xy} + \xi_y \tau_{yy} + \xi_z \tau_{yz} \\ \xi_x \tau_{xz} + \xi_y \tau_{yz} + \xi_z \tau_{zz} \\ \xi_x \beta_x + \xi_y \beta_y + \xi_z \beta_z \end{pmatrix}, \quad (34)$$

$$\hat{\mathbf{F}}_v = J^{-1} \begin{pmatrix} 0 \\ \eta_x \tau_{xx} + \eta_y \tau_{xy} + \eta_z \tau_{xz} \\ \eta_x \tau_{xy} + \eta_y \tau_{yy} + \eta_z \tau_{yz} \\ \eta_x \tau_{xz} + \eta_y \tau_{yz} + \eta_z \tau_{zz} \\ \eta_x \beta_x + \eta_y \beta_y + \eta_z \beta_z \end{pmatrix}, \quad (35)$$

$$\hat{\mathbf{G}}_v = J^{-1} \begin{pmatrix} 0 \\ \zeta_x \tau_{xx} + \zeta_y \tau_{xy} + \zeta_z \tau_{xz} \\ \zeta_x \tau_{xy} + \zeta_y \tau_{yy} + \zeta_z \tau_{yz} \\ \zeta_x \tau_{xz} + \zeta_y \tau_{yz} + \zeta_z \tau_{zz} \\ \zeta_x \beta_x + \zeta_y \beta_y + \zeta_z \beta_z \end{pmatrix}, \quad (36)$$

where β_x , β_y and β_z are defined as

$$\begin{aligned} \beta_x &= \tau_{xx} \tilde{u} + \tau_{xy} \tilde{v} + \tau_{xz} \tilde{w} - \bar{q}_x, \\ \beta_y &= \tau_{xy} \tilde{u} + \tau_{yy} \tilde{v} + \tau_{yz} \tilde{w} - \bar{q}_y, \\ \beta_z &= \tau_{xz} \tilde{u} + \tau_{yz} \tilde{v} + \tau_{zz} \tilde{w} - \bar{q}_z. \end{aligned} \quad (37)$$

V. Dimensionless Formulation

A convenient nondimensionalization is necessary in to order to achieve a consistent implementation of the governing equations of motion. Dimensionless formulation yields to a more general numerical tool. There is no need to change the formulation for each configuration intended to be simulated. Moreover, dimensionless formulation scales all the necessary properties to the same order of magnitude which is a computational advantage.²⁶ Dimensionless variables are presented in the present section in order perform the nondimensionalization of Eq. (25)

The dimensionless time, \underline{t} , is written as function of the speed of sound of the jet at the inlet, a_j , and of a reference lenght, l ,

$$\underline{t} = t \frac{a_j}{l}. \quad (38)$$

The dimensionless velocity components are obtained using the speed of sound of the jet at the inlet,

$$\underline{\mathbf{u}} = \frac{\mathbf{u}}{a_j}. \quad (39)$$

Dimensionless pressure and energy are calculated using density and speed of the sound of the jet at the inlet as

$$\underline{p} = \frac{p}{\rho_j a_j^2}, \quad (40)$$

$$\underline{E} = \frac{E}{\rho_j a_j^2}. \quad (41)$$

Dimensionless density, $\underline{\rho}$, temperature, \underline{T} and viscosity, $\underline{\mu}$, are calculated using freestream properties

$$\underline{\rho} = \frac{\rho}{\rho_j}. \quad (42)$$

One can use the dimensionless properties described above in order to write the dimensionless form of the RANS equations as

$$\frac{\partial Q}{\partial t} + \frac{\partial \underline{\mathbf{E}}_e}{\partial \xi} + \frac{\partial \underline{\mathbf{F}}_e}{\partial \eta} + \frac{\partial \underline{\mathbf{G}}_e}{\partial \zeta} = \frac{M_j}{Re} \left(\frac{\partial \underline{\mathbf{E}}_v}{\partial \xi} + \frac{\partial \underline{\mathbf{F}}_v}{\partial \eta} + \frac{\partial \underline{\mathbf{G}}_v}{\partial \zeta} \right), \quad (43)$$

where the underlined terms are calculated using dimensionless properties. The Mach number of the jet, M_j , and the Reynolds number are based on the mean inlet velocity of the jet, U_j , diameter of the inlet, D , and freestream properties such as speed of sound, a_∞ , density, ρ_∞ and viscosity, μ_∞ ,

$$M_j = \frac{U_j}{a_\infty} \quad \text{and} \quad Re = \frac{\rho_j U_j D}{\mu_j}. \quad (44)$$

VI. Numerical Formulation

The governing equations previously described are discretized in a structured finite difference context for general curvilinear coordinate system.²⁶ The numerical flux is calculated through a central difference scheme with the explicit addition of the anisotropic scalar artificial dissipation of Turkel and Vatsa.²⁷ The time integration is performed by an explicit, 2nd-order, 5-stage Runge-Kutta scheme.^{28,29} Conserved properties and artificial dissipation terms are properly treated near boundaries in order to assure the physical correctness of the numerical formulation.

VI.A. Spatial Discretization

For the sake of simplicity the formulation discussed in the present section is no longer written using bars. However, the reader should notice that the equations are dimensionless and filtered. The Navier-Stokes equations, presented in Eq. (43), are discretized in space in a finite difference fashion and, then, rewritten as

$$\left(\frac{\partial Q}{\partial t} \right)_{i,j,k} = -RHS_{i,j,k}, \quad (45)$$

where RHS is the right hand side of the equation and it is written as function of the numerical flux vectors at the interfaces between grid points,

$$\begin{aligned} RHS_{i,j,k} = & \frac{1}{\Delta \xi} \left(\mathbf{E}_{e(i+\frac{1}{2},j,k)} - \mathbf{E}_{e(i-\frac{1}{2},j,k)} - \mathbf{E}_{v(i+\frac{1}{2},j,k)} + \mathbf{E}_{v(i-\frac{1}{2},j,k)} \right) \\ & \frac{1}{\Delta \eta} \left(\mathbf{F}_{e(i,j+\frac{1}{2},k)} - \mathbf{F}_{e(i,j-\frac{1}{2},k)} - \mathbf{F}_{v(i,j+\frac{1}{2},k)} + \mathbf{F}_{v(i,j-\frac{1}{2},k)} \right) \\ & \frac{1}{\Delta \zeta} \left(\mathbf{G}_{e(i,j,k+\frac{1}{2})} - \mathbf{G}_{e(i,j,k-\frac{1}{2})} - \mathbf{G}_{v(i,j,k+\frac{1}{2})} + \mathbf{G}_{v(i,j,k-\frac{1}{2})} \right). \end{aligned} \quad (46)$$

For the general curvilinear coordinate case $\Delta \xi = \Delta \eta = \Delta \zeta = 1$. The anisotropic scalar artificial dissipation method of Turkel and Vatsa²⁷ is implemented through the modification of the inviscid flux vectors, \mathbf{E}_e , \mathbf{F}_e and \mathbf{G}_e . The numerical scheme is nonlinear and allows the selection between artificial dissipation terms of second and fourth differences, which is very important for capturing discontinuities in the flow. The numerical fluxes are calculated at interfaces in order to reduce the size of the calculation cell and, therefore, facilitate the implementation of second derivatives since the the concept of numerical fluxes vectors is used for flux

differencing. Only internal interfaces receive the corresponding artificial dissipation terms, and differences of the viscous flux vectors use two neighboring points of the interface.

The inviscid flux vectors, with the addition of the artificial dissipation contribution, can be written as

$$\begin{aligned}\mathbf{E}_{e(i\pm\frac{1}{2},j,k)} &= \frac{1}{2} (\mathbf{E}_{e(i,j,k)} + \mathbf{E}_{e(i\pm 1,j,k)}) - J^{-1} \mathbf{d}_{(i\pm\frac{1}{2},j,k)}, \\ \mathbf{F}_{e(i,j,\pm\frac{1}{2},k)} &= \frac{1}{2} (\mathbf{F}_{e(i,j,k)} + \mathbf{F}_{e(i,j,\pm 1,k)}) - J^{-1} \mathbf{d}_{(i,j,\pm\frac{1}{2},k)}, \\ \mathbf{G}_{e(i,j,k\pm\frac{1}{2})} &= \frac{1}{2} (\mathbf{G}_{e(i,j,k)} + \mathbf{G}_{e(i,j,k\pm 1)}) - J^{-1} \mathbf{d}_{(i,j,k\pm\frac{1}{2})},\end{aligned}\quad (47)$$

in which the $\mathbf{d}_{(i\pm 1,j,k)}$, $\mathbf{d}_{(i,j,\pm 1,k)}$ and $\mathbf{d}_{(i,j,k\pm 1)}$ terms are the Turkel and Vatsa²⁷ artificial dissipation terms in the i , j , and k directions respectively. The scaling of the artificial dissipation operator in each coordinate direction is weighted by its own spectral radius of the corresponding flux Jacobian matrix, which gives the non-isotropic characteristics of the method.²⁶ The artificial dissipation contribution in the ξ direction is given by

$$\begin{aligned}\mathbf{d}_{(i+\frac{1}{2},j,k)} &= \lambda_{(i+\frac{1}{2},j,k)} \left[\epsilon_{(i+\frac{1}{2},j,k)}^{(2)} (\mathcal{W}_{(i+1,j,k)} - \mathcal{W}_{(i,j,k)}) \right. \\ &\quad \left. \epsilon_{(i+\frac{1}{2},j,k)}^{(4)} (\mathcal{W}_{(i+2,j,k)} - 3\mathcal{W}_{(i+1,j,k)} + 3\mathcal{W}_{(i,j,k)} - \mathcal{W}_{(i-1,j,k)}) \right],\end{aligned}\quad (48)$$

in which

$$\epsilon_{(i+\frac{1}{2},j,k)}^{(2)} = k^{(2)} \max \left(\nu_{(i+1,j,k)}^d, \nu_{(i,j,k)}^d \right), \quad (49)$$

$$\epsilon_{(i+\frac{1}{2},j,k)}^{(4)} = \max \left[0, k^{(4)} - \epsilon_{(i+\frac{1}{2},j,k)}^{(2)} \right]. \quad (50)$$

The original article²⁷ recommends using $k^{(2)} = 0.25$ and $k^{(4)} = 0.016$ for the dissipation artificial constants. The pressure gradient sensor, $\nu_{(i,j,k)}^d$, for the ξ direction is written as

$$\nu_{(i,j,k)}^d = \frac{|p_{(i+1,j,k)} - 2p_{(i,j,k)} + p_{(i-1,j,k)}|}{p_{(i+1,j,k)} - 2p_{(i,j,k)} + p_{(i-1,j,k)}}. \quad (51)$$

The \mathcal{W} vector from Eq. (48) is calculated as a function of the conserved variable vector, \hat{Q} , written in Eq. (27). The formulation intends to keep the total enthalpy constant in the final converged solution, which is the correct result for the Navier-Stokes equations with $Re \rightarrow \infty$. This approach is also valid for the viscous formulation because the dissipation terms are added to the inviscid flux terms, in which they are really necessary to avoid nonlinear instabilities of the numerical formulation. The \mathcal{W} vector is given by

$$\mathcal{W} = \hat{Q} + [0 \ 0 \ 0 \ 0 \ p]^T. \quad (52)$$

The spectral radius-based scaling factor, λ , for the i -th direction is written

$$\lambda_{(i+\frac{1}{2},j,k)} = \frac{1}{2} \left[(\overline{\lambda_\xi})_{(i,j,k)} + (\overline{\lambda_\xi})_{(i+1,j,k)} \right], \quad (53)$$

where

$$\overline{\lambda_\xi}_{(i,j,k)} = \lambda_\xi \left[1 + \left(\frac{\lambda_\eta}{\lambda_\xi} \right)^{0.5} + \left(\frac{\lambda_\zeta}{\lambda_\xi} \right)^{0.5} \right]. \quad (54)$$

The spectral radii, λ_ξ , λ_η and λ_ζ are given by

$$\begin{aligned}\lambda_\xi &= |U| + a\sqrt{\xi_x^2 + \eta_y^2 + \zeta_z^2}, \\ \lambda_\eta &= |V| + a\sqrt{\xi_x^2 + \eta_y^2 + \zeta_z^2}, \\ \lambda_\zeta &= |W| + a\sqrt{\xi_x^2 + \eta_y^2 + \zeta_z^2},\end{aligned}\quad (55)$$

in which, U , V and W are the contravariants velocities in the ξ , η and ζ , previously written in Eq. (32), and a is the local speed of sound, which can be written as

$$a = \sqrt{\frac{\gamma p}{\rho}}. \quad (56)$$

The calculation of artificial dissipation terms for the other coordinate directions are completely similar and, therefore, they are not discussed in the present work.

VI.B. Time Marching Method

The time marching method used in the present work is a 2nd-order, 5-step Runge-Kutta scheme based on the work of Jameson.^{28,29} The time integration can be written as

$$\begin{aligned} Q_{(i,jk,)}^{(0)} &= Q_{(i,jk,)}^{(n)}, \\ Q_{(i,jk,)}^{(l)} &= Q_{(i,jk,)}^{(0)} - \alpha_l \Delta t_{(i,j,k)} RHS_{(i,j,k)}^{(l-1)} \quad l = 1, 2 \dots 5, \\ Q_{(i,jk,)}^{(n+1)} &= Q_{(i,jk,)}^{(5)}, \end{aligned} \quad (57)$$

in which Δt is the time step and n and $n + 1$ indicate the property values at the current and at the next time step, respectively. The literature^{28,29} recommends

$$\alpha_1 = \frac{1}{4}, \quad \alpha_2 = \frac{1}{6}, \quad \alpha_3 = \frac{3}{8}, \quad \alpha_4 = \frac{1}{2}, \quad \alpha_5 = 1, \quad (58)$$

in order to improve the numerical stability of the time integration. The present scheme is theoretically stable for $CFL \leq 2\sqrt{2}$, under a linear analysis.²⁶

VII. Boundary Conditions

The geometry used in the present work presents a cylindrical shape which is generated by the rotation of a 2-D plan around a centerline. Figure 1 presents a lateral view and a frontal view of the computational domain used in the present work and the positioning of the entrance, exit, centerline, far field and periodic boundary conditions. A discussion on all boundary conditions is performed in the following subsections.

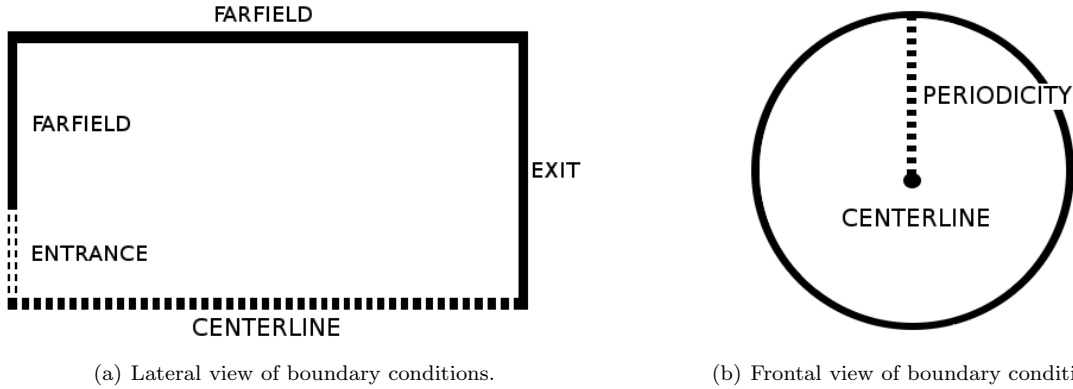


Figure 1. Lateral and frontal views of the computational domain indicating boundary conditions.

VII.A. Far Field Boundary

Riemann invariants³⁰ are used to implement far field boundary conditions. They are derived from the characteristic relations for the Euler equations. At the interface of the outer boundary, the following expressions apply

$$\mathbf{R}^- = \mathbf{R}_\infty^- = q_{n_\infty} - \frac{2}{\gamma - 1} a_\infty, \quad (59)$$

$$\mathbf{R}^+ = \mathbf{R}_e^+ = q_{n_e} - \frac{2}{\gamma - 1} a_e, \quad (60)$$

where ∞ and e indexes stand for the property in the freestream and in the internal region, respectively. q_n is the velocity component normal to the outer surface, defined as

$$q_n = \mathbf{u} \cdot \vec{n}, \quad (61)$$

and \vec{n} is the unit outward normal vector

$$\vec{n} = \frac{1}{\sqrt{\eta_x^2 + \eta_y^2 + \eta_z^2}} [\eta_x \ \eta_y \ \eta_z]^T. \quad (62)$$

Equation (61) assumes that the η direction is pointing from the jet to the external boundary. Solving for q_n and a , one can obtain

$$q_{nf} = \frac{\mathbf{R}^+ + \mathbf{R}^-}{2}, \quad a_f = \frac{\gamma - 1}{4} (\mathbf{R}^+ - \mathbf{R}^-). \quad (63)$$

The index f is linked to the property at the boundary surface and will be used to update the solution at this boundary. For a subsonic exit boundary, $0 < q_{ne}/a_e < 1$, the velocity components are derived from internal properties as

$$\begin{aligned} u_f &= u_e + (q_{nf} - q_{ne})\eta_x, \\ v_f &= v_e + (q_{nf} - q_{ne})\eta_y, \\ w_f &= w_e + (q_{nf} - q_{ne})\eta_z. \end{aligned} \quad (64)$$

Density and pressure properties are obtained by extrapolating the entropy from the adjacent grid node,

$$\rho_f = \left(\frac{\rho_e^\gamma a_f^2}{\gamma p_e} \right)^{\frac{1}{\gamma-1}}, \quad p_f = \frac{\rho_f a_f^2}{\gamma}.$$

For a subsonic entrance, $-1 < q_{ne}/a_e < 0$, properties are obtained similarly from the freestream variables as

$$\begin{aligned} u_f &= u_\infty + (q_{nf} - q_{n\infty})\eta_x, \\ v_f &= v_\infty + (q_{nf} - q_{n\infty})\eta_y, \\ w_f &= w_\infty + (q_{nf} - q_{n\infty})\eta_z, \end{aligned} \quad (65)$$

$$\rho_f = \left(\frac{\rho_\infty^\gamma a_f^2}{\gamma p_\infty} \right)^{\frac{1}{\gamma-1}}. \quad (66)$$

For a supersonic exit boundary, $q_{ne}/a_e > 1$, the properties are extrapolated from the interior of the domain as

$$\begin{aligned} \rho_f &= \rho_e, \\ u_f &= u_e, \\ v_f &= v_e, \\ w_f &= w_e, \\ e_f &= e_e, \end{aligned} \quad (67)$$

and for a supersonic entrance, $q_{ne}/a_e < -1$, the properties are extrapolated from the freestream variables as

$$\begin{aligned} \rho_f &= \rho_\infty, \\ u_f &= u_\infty, \\ v_f &= v_\infty, \\ w_f &= w_\infty, \\ e_f &= e_\infty. \end{aligned} \quad (68)$$

VII.B. Entrance Boundary

For a jet-like configuration, the entrance boundary is divided in two areas: the jet and the area above it. The jet entrance boundary condition is implemented through the use of the 1-D characteristic relations for the 3-D Euler equations for a flat velocity profile. The set of properties then determined is computed from within and from outside the computational domain. For the subsonic entrance, the v and w components of the velocity are extrapolated by a zero-order extrapolation from inside the computational domain and the angle of flow entrance is assumed fixed. The rest of the properties are obtained as a function of the jet Mach number, which is a known variable.

$$\begin{aligned} (u)_{1,j,k} &= u_j, \\ (v)_{1,j,k} &= (v)_{2,j,k}, \\ (w)_{1,j,k} &= (w)_{2,j,k}. \end{aligned} \quad (69)$$

The dimensionless total temperature and total pressure are defined with the isentropic relations:

$$T_t = 1 + \frac{1}{2}(\gamma - 1)M_\infty^2 \quad \text{and} \quad P_t = \frac{1}{\gamma}(T_t)^{\frac{\gamma}{\gamma-1}}. \quad (70)$$

The dimensionless static temperature and pressure are deduced from Eq. (70), resulting in

$$(T)_{1,j,k} = \frac{T_t}{1 + \frac{1}{2}(\gamma - 1)(u^2 + v^2 + w^2)_{1,j,k}} \quad \text{and} \quad (p)_{1,j,k} = \frac{1}{\gamma}(T)_{1,j,k}^{\frac{\gamma}{\gamma-1}}. \quad (71)$$

For the supersonic case, all conserved variables receive jet property values.

The far field boundary conditions are implemented outside of the jet area in order to correctly propagate information coming from the inner domain of the flow to the outer region of the simulation. However, in the present case, ξ , instead of η , as presented in the previous subsection, is the normal direction used to define the Riemann invariants.

VII.C. Exit Boundary Condition

At the exit plane, the same reasoning of the jet entrance boundary is applied. This time, for a subsonic exit, the pressure is obtained from the outside and all other variables are extrapolated from the interior of the computational domain by a zero-order extrapolation. The conserved variables are obtained as

$$(\rho)_{I_{MAX},j,k} = \frac{(p)_{I_{MAX},j,k}}{(\gamma - 1)(e)_{I_{MAX}-1,j,k}}, \quad (72)$$

$$(\vec{u})_{I_{MAX},j,k} = (\vec{u})_{I_{MAX}-1,j,k}, \quad (73)$$

$$(e_i)_{I_{MAX},j,k} = (\rho)_{I_{MAX},j,k} \left[(e)_{I_{MAX}-1,j,k} + \frac{1}{2}(\vec{u})_{I_{MAX},j,k} \cdot (\vec{u})_{I_{MAX},j,k} \right], \quad (74)$$

in which I_{MAX} stands for the last point of the mesh in the axial direction. For the supersonic exit, all properties are extrapolated from the interior domain.

VII.D. Centerline Boundary Condition

The centerline boundary is a singularity of the coordinate transformation, and, hence, an adequate treatment of this boundary must be provided. The conserved properties are extrapolated from the adjacent longitudinal plane and are averaged in the azimuthal direction in order to define the updated properties at the centerline of the jet.

The fourth-difference terms of the artificial dissipation scheme, used in the present work, are carefully treated in order to avoid the five-point difference stencils at the centerline singularity. If one considers the flux balance at one grid point near the centerline boundary in a certain coordinate direction, let w_j denote a component of the \mathcal{W} vector from Eq. (52) and \mathbf{d}_j denote the corresponding artificial dissipation term at the mesh point j . In the present example, $(\Delta w)_{j+\frac{1}{2}}$ stands for the difference between the solution at the interface for the points $j+1$ and j . The fourth-difference of the dissipative fluxes from Eq. (48) can be written as

$$\mathbf{d}_{j+\frac{1}{2}} = (\Delta w)_{j+\frac{3}{2}} - 2(\Delta w)_{j+\frac{1}{2}} + (\Delta w)_{j-\frac{1}{2}}. \quad (75)$$

Considering the centerline and the point $j = 1$, as presented in Fig. 2, the calculation of $\mathbf{d}_{1+\frac{1}{2}}$ demands the $(\Delta w)_{\frac{1}{2}}$ term, which is unknown since it is outside the computation domain. In the present work a extrapolation is performed and given by

$$(\Delta w)_{\frac{1}{2}} = -(\Delta w)_{1+\frac{1}{2}} . \quad (76)$$

This extrapolation modifies the calculation of $\mathbf{d}_{1+\frac{1}{2}}$ that can be written as

$$\mathbf{d}_{j+\frac{1}{2}} = (\Delta w)_{j+\frac{3}{2}} - 3(\Delta w)_{j+\frac{1}{2}} . \quad (77)$$

The approach is plausible since the centerline region is smooth and does not have high gradient of properties.

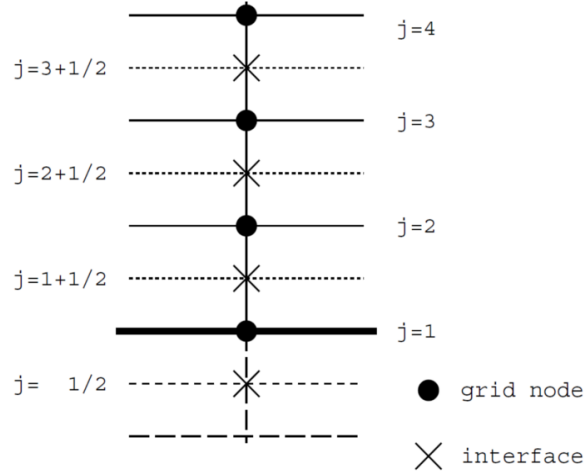


Figure 2. Boundary points dissipation.²⁶

VII.E. Periodic Boundary Condition

A periodic condition is implemented between the first ($K = 1$) and the last point in the azimuthal direction ($K = K_{MAX}$) in order to close the 3-D computational domain. There are no boundaries in this direction, since all the points are inside the domain. The first and the last points, in the azimuthal direction, are superposed in order to facilitate the boundary condition implementation which is given by

$$\begin{aligned} (\rho)_{i,j,K_{MAX}} &= (\rho)_{i,j,1} , \\ (u)_{i,j,K_{MAX}} &= (u)_{i,j,1} , \\ (v)_{i,j,K_{MAX}} &= (v)_{i,j,1} , \\ (w)_{i,j,K_{MAX}} &= (w)_{i,j,1} , \\ (e)_{i,j,K_{MAX}} &= (e)_{i,j,1} . \end{aligned} \quad (78)$$

VIII. High Performance Computing

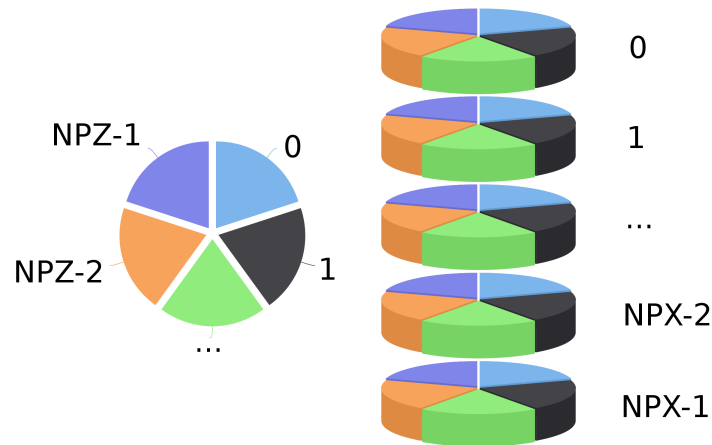
The current section presents an overview of the LES solver and discusses the high performance computing implementations introduced into the code. A study on the parallel performance of JAZzY using multiple processors is presented and discussed in the end of the section.

VIII.A. Mesh Generation

The LES solver presents a parallel-IO feature in which each MPI partition reads its correspondent portion of the mesh. Therefore, a 3-D grid generator is developed in order to provide partitioned CGNS mesh files to

the LES solver. The CGNS standard⁹⁻¹¹ is build on the HDF5 library.^{7,8} This library is a general scientific format adaptable to virtually any scientific or engineering application. It provides tools to efficiently read and write data structured in a binary tree fashion. This data structure can handle many types of queries very efficiently^{31,32} such as time-dependent CFD solution.

Figure 3(a) illustrates the segmentation of the domain into the axial and azimuthal directions while Fig. 3(b) presents the mapping of the domain. The index of each partition, indicated in Fig. 3(b), is based on a matrix index system in which the rows represent the position in the axial direction and the columns represent the position in the azimuthal direction. The partition index starts at zero to be consistent with the message passing interface standard. NPX and NPZ denote the number of partitions in the axial and azimuthal directions, respectively.



(a) 2-D partitioning in the axial and azimuthal direction.

0	NPZ	2*NPZ		
1	NPZ+1	2*NPZ+1		
...	$j*(NPZ)+i$...
NPZ-2	NPZ+NPZ-2	2*NPZ+NPZ-2		
NPZ-1	NPZ+NPZ-1	2*NPZ+NPZ-1		NPX*NPZ-1

(b) Mapping of the 2-D partitioning.

Figure 3. 2-D partitioning and mapping.

Table 1 presents the algorithm of the mesh generator. The user can provide geometry and mesh point distribution parameters so the grid generator can create a 2-D mesh. A complete 2-D grid, from a different mesh generator, can also be provided by the user to the mesh generator. In the sequence, the 2-D grid is partitioned in the axial direction. After the partitioning in the axial direction, each portion of the mesh is

extruded in the azimuthal direction respecting the positioning of the MPI partitions. Each portion of the mesh is written using the CGNS standard.

Table 1. Mesh generator overview.

1	BEGIN
2	Read input data
3	Read mesh or create 2-D mesh
4	Perform balanced partitioning in axial direction
5	Perform balanced partitioning in azimuthal direction
6	Rotate the mesh partition in the azimuthal direction
7	Write a CGNS mesh file for each partition
8	END

The division of the mesh in the axial and azimuthal directions is performed towards a well balanced distribution of points. Firstly, the total number of grid points in one direction is divided by the number of domains in the same direction. The remaining points are spread among the partitions in the case which the division is not exact. Figure 4 illustrates the balancing procedure performed in each direction during the partitioning of the computational grid.

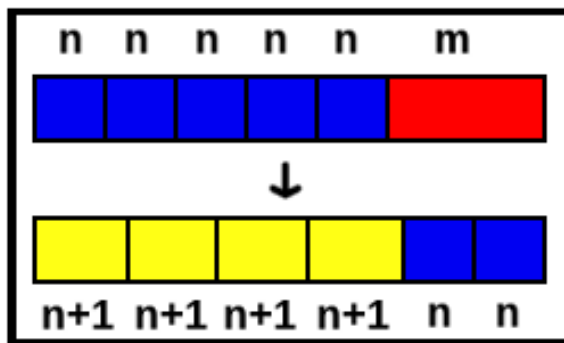


Figure 4. Balancing procedure performed during the partitioning of the mesh.

VIII.B. JAZzY Overview

JAZzY is the LES solver presented in the current work. Table 2 presents a brief overview of JAZzY. In the beginning of the calculation every MPI partition reads the same ASCII file which provides input data such as flow configurations and simulation settings. In the sequence, each MPI partition reads its correspondent CGNS mesh file. The Jacobian and the metric terms are calculated after the I-O procedure. Then, each processor sets the initial conditions defined in the input data and it performs an asynchronous communication before starting iterations in order to solve the compressible LES equations.

The first operation, which is performed in the iteration loop, is the computation of the inviscid flux vectors. Then, the artificial dissipation operator is calculated. Asynchronous communications are performed during this computation. After the data exchange, the inviscid terms of the LES formulation is calculated using the convective operator and the artificial dissipation terms. The viscous terms are calculated in sequence and their contributions are added to the right-hand side of the LES equations.

The time integration is performed using a five step Runge-Kutta time integration scheme after the calculation of the numerical fluxes. This time marching scheme calculates the inviscid and viscous terms recursively through the inner steps. Therefore, multiple communications are performed during the time integration. The solution, boundary conditions and fluid viscosity are updated after the time marching. Asynchronous communications are performed for the periodicity condition. Blocking communications are performed in order to calculate properties at the centerline singularity. After the updates, neighbor partitions

Table 2. The JAZzY code overview.

1	Read input data
2	Read mesh
3	Calculate Jacobian
4	Calculate metric terms
5	Set up initial conditions
6	Asynchronous communication
7	WHILE (it. < max nb it.)
	Compute inviscid flux vectors
	Compute artificial dissipation operator
	Calculate inviscid flux contributions to the residue
	Compute viscous flux vectors and SGS viscosity
	Calculate viscous flux contributions to the residue
	Calculate time step
	Perform multi-step explicit time integration
	Update the solution and boundary conditions
8	END WHILE
9	Output results
10	END

exchange data using non blocking MPI routines. The SGS viscosity is calculated in the end of the iteration loop. The Vreman and the static Smagorinsky models does not request the use of communications. The calculation of the dynamic Smagorinsky SGS viscosity is performed using blocking data exchange in order to calculate properties on the second level filtering. Finally, when the requested number of iterations is achieved, each MPI partition appends the solution to the output CGNS file.

VIII.C. Communication

Numerical data exchange between the partitions is necessary in order to perform parallel computation. Ghost points are added to the boundaries of local partition mesh at the main flow direction and at the azimuthal direction in order to carry information of the neighbor points. The artificial dissipation scheme implemented in the code²⁸ uses a five points stencil which demands information of the two neighbors of a given mesh point. Hence, a two layer ghost points is created at the beginning and at the end of each partition. Figure 5 presents the layer of ghost points used in the present code. The yellow and black layers represent the axial and azimuthal ghost points respectively. The green region is the partition mesh.

After the ghost points creation, each processor performs the computation. Communication between neighbor partitions are performed in order to allow data information pass through the computational domain. Blocking and non-blocking communications are used in the present work. In the blocking communication approach, the partition which sends the information only restarts the computation after the neighbor partition, which is the receiver, has finished to read the data. The same does not occur for non-blocking communications. The partition which has sent data does not need to wait a signal from the receiver. The developer is responsible to assure that data is communicated before being accessed through the use of MPI wait functions along the code. Most of the data exchange are performed using non-blocking MPI communication routines in the current research. Only the centerline boundary condition and the communications for the dynamic Smagorinsky model^{24,33} are performed using blocking MPI communication routines. The first is performed in order to assure reproducibility of the solver. The second is performed using blocking communication because it represents only a small portion of the code.

The meshes used in the current research have a singularity at the centerline. It is necessary to correctly treat this region for the sake of data consistency. Therefore, properties are extrapolated to the singularity in radial direction and, in the sequence, the master partition collects all data from the partitions that share the

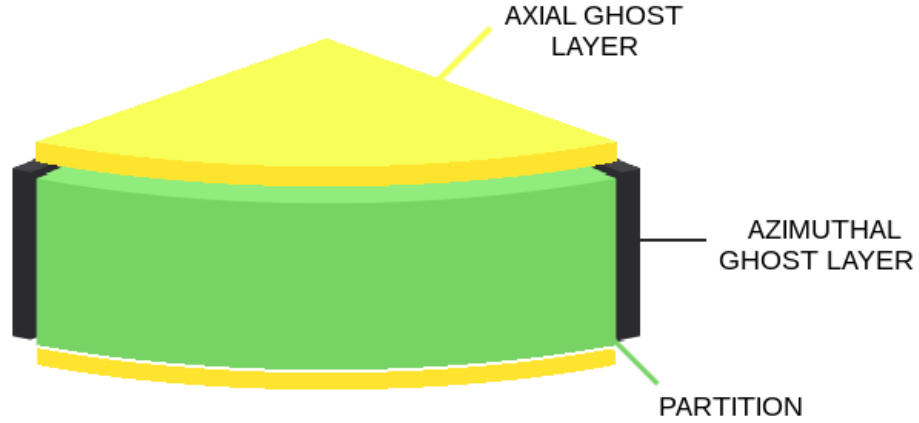


Figure 5. Ghost points creation procedure.

same singularity point and allocates into one single vector. After the allocation, the properties are averaged in a sequential fashion and the result is spread to the neighbors in the azimuthal direction. Figure 6 illustrates the singularity treatment for a configuration with 16 points in the azimuthal direction. The yellow, red, blue and green colors represent the four partitions in the azimuthal direction. Such procedure does not use collective communications in order to preserve the commutative property during the averaging. This blocking communication is very important in order to achieve the binary reproducibility of the computational tool.³⁴ The use of such communication is motivated by the work of Arteaga *et. al.*³⁵

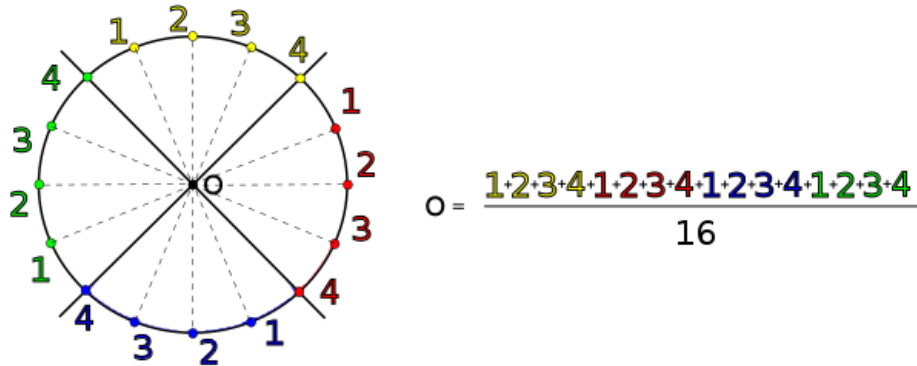
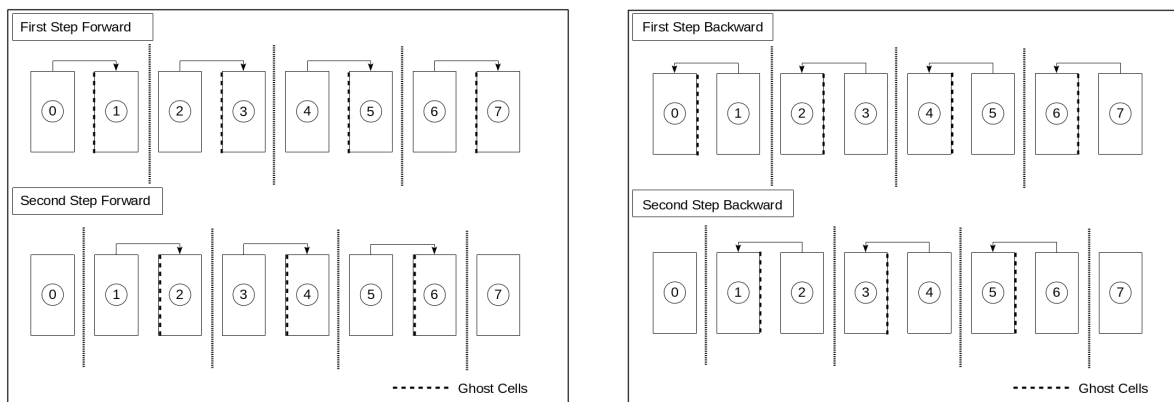


Figure 6. Singularity averaging in parallel.

Non-blocking communication is not available for the communication performed by the dynamic Smagorinsky model. Only blocking communication are implemented because it represents only a small portion of the code. This data exchange is firstly performed in the azimuthal direction and in the sequence in the axial direction. The azimuthal communication is performed in four blocking steps as Figs. 7(a) and 7(b) demonstrate. Initially, the communication is performed in the forward direction. Even partitions send information of their two last local layers to the ghost points at the left of odd partitions. If the last partition is even, it does not share information in this step. In the sequence, odd partitions send information of their two last local layers to the ghost points at the left of even partitions. If the last partition is odd, it does not share information in this step. The third and the fourth steps are backward communications. First, odd

partitions send data of their two first local layers to the ghost points at the right of even partitions. Finally, all even partitions, but the first, send data of their two first local layers to the ghost points at the right of odd partitions. Communication in the axial direction are performed using the same approach.



(a) Forward communication between partitions.

(b) Backward Communication between partitions.

Figure 7. Forward and Backward communication schemes used in order to exchange information between neighbor partitions

VIII.D. Computational Resources

The current work is included into a national project know as CEPID-CeMEAI.³⁶ This project provides access to a SGI cluster. The machine has 104 computational nodes and each one has two deca-core 2.8 GHz *Intel Xeon*[®] E52680v2 processors and 128 Gb DDR3 1866MHz random access memory. The entire cluster has 2080 computational cores available for the project members. The storage can be performed using the network file system (NFS) or the *Lustre*[®] file system.³⁷ Both storage system have 175 Tb available for the users. The network communication is performed using Infiniband and Gigabit Ethernet. The Operational system is the Red Hat Enterprise Linux³⁸ and the job scheduler is the Altair PBS Pro.³⁹

The Intel Composer XE Update 2 compiler, version 15.0.2.164 is used in the present work. The code is compiled using optimization flags in order to achieve the best computational performance. The best compilation flags were tested in the present work. The flags which provided the best results are:

- O3: enables aggressive optimization such as global code scheduling, software pipelining, predication and speculation, prefetching, scalar replacement and loop transformations;
- xHost: tells the compiler to generate instructions for the highest instruction set available on the compilation host processor;
- ipo: automatic, multi-step process that allows the compiler to analyze the code and determine where you can benefit from specific optimizations;
- no-prec-div: enables optimizations that give slightly less precise results than full division;
- assume buffered.io : tells the compiler to accumulate records in a buffer;
- override-limits: deals with very large, complex functions and loops.

VIII.E. Computational Performance

Parallel computation can largely decrease the time of CFD simulations. However, the parallel upgrade of a serial solver must be carefully performed. The communication between partitions is not free and can affect the computational performance in parallel. The partitioning of the computational domain increases the number of communication between processors. When the number of points of a partitions becomes smaller

simulation spend less time computing and more time performing communications. Consequently, the parallel performance of the solver is deteriorated.

The speedup is one of the most common figures for the performance evaluation of parallel algorithms and architectures⁴⁰ and it is used in the present work in order to measure the computational performance of the parallel solver and compare with the ideal case. Different approaches are used by the scientific community in order to calculate the speedup.^{41,42} In the present work the speedup, Sp_N , is given by

$$Sp_N = \frac{T_s}{T_N}. \quad (79)$$

in which T_N and T_s stand for the time spent to perform one thousand iterations using N processors and one single processor, respectively. The efficiency as function of the number of processors, η_N , is written considering Amdahl's law⁴³ as

$$\eta_N = \frac{Sp_N}{N}. \quad (80)$$

The performance of the solver is evaluated for a large-eddy simulation of a isothermic perfectly expanded turbulent jet flow without any SGS model. The impact of SGS models on the parallel performance of the code is evaluated in the work of Junqueira-Junior.¹ Different parameters such as mesh size, partitioning configurations and number of processors are used to study the parallel behavior of the code in the current article.

Table 3 presents the different grid configurations used in the current work. There are nine meshes whose total number of points doubles every time. The first column presents the name of the mesh. The second, third and fourth columns present the number of points in the axial, radial and azimuthal directions, respectively. The last column indicates the total number of points of the mesh. The grid point distribution in the azimuthal direction is fixed and it is equals to 361. The smallest grid, named as Mesh A, has approximately 5.9 million points while the biggest grid presents approximately 1.0 billion points.

Table 3. Configuration of computational meshes used in the current study.

Mesh	No. Pt. Axial Direct.	No. Pt. Radial Direct.	No. Pt. Azimut. Direct.	No. Pt.
A	128	128	361	5.9M
B	256	128	361	11.8M
C	256	256	361	23.7M
D	512	256	361	47.3M
E	512	512	361	94.6M
F	1024	512	361	189.3M
G	1024	1024	361	378.5M
H	2048	1024	361	757.1M
I	1700	1700	361	1.0B

The strong scalability test is used in the present paper in order to evaluate the parallel performance of the code. This test is a measure of the evolution of speedup and efficiency of a given problem, with a fixed size, as the number of processors increases. Simulations are performed using up to 400 processors in the present paper. Different partitioning configurations are used in order to measure its effects on the parallel computational efficiency. Table 4 presents the number of partitions in the azimuthal direction for each number of processors used to study the scalability of the solver. The first column indicates the computational resource while the second columns indicates the number of zones in the azimuthal direction used to evaluate the effects of the partitioning on the computation.

Isothermic perfectly expanded jet flow simulations are performed using different grid sizes and different partition configurations. The Reynolds number of the jet is 1.5744×10^6 for the present simulations and a flat-hat profile with Mach number of 1.4 is imposed at the entrance of the computational domain. A stagnated flow is used as initial condition for the simulations. The time increment is 2.5×10^{-4} seconds for the tests performed. Numerical results of such configuration using the same code are presented in the work described in Ref. [2, 44]. In the present article each simulation performs 1000 iterations or 24 hours

Table 4. Number of partitions in the azimuthal direction for a given number of processors.

No. Proc.	No. of Part. in the Azimuthal Dir.							
1	1							
2	1				2			
5	1				5			
10	1		2	5	10			
20	1	2	4	5	10	20		
40	1	2	4	5	8	10	20	40
80	2	4	5	8	10	20	40	
100	2	4	5	10	20	25		
200	4	8	10	20	25	50		
400	8	16	20	25	50			

of computation. An average of the CPU time per iteration through the simulations is measured in order to calculate and compare computational cost, speed-up and efficiency of the solver.

Tables 5 to 13 present, for a given number of processors, the partitioning configuration which provides the best averaged CPU time per iteration, its correspondent speedup and its correspondent computational efficiency for meshes A to I respectively. One can notice that meshes F,G,H and I are too big and cannot fit into one single node of the computational cluster used in the current paper. The scalability study started with 40 processors for mesh F, 80 processors for mesh G, and 200 processors for mesh H and mesh I. The efficiency of the solver is considered 100% at the starting point in order to have a reference for the cases in which is not possible to perform a simulation using one single computational core.

Table 5. Computational performance of Mesh A.

No. Proc.	Av. CPU time	Speedup	Efficiency	No. Azim. Part.
1	2.97E+01	1.00E+00	1.00E+00	1
2	1.14E+01	2.61E+00	1.31E+00	1
5	3.96E+00	7.49E+00	1.50E+00	1
10	2.27E+00	1.31E+01	1.31E+00	2
20	1.57E+00	1.89E+01	9.43E-01	5
40	8.32E-01	3.57E+01	8.91E-01	20
80	4.60E-01	6.45E+01	8.07E-01	20
100	3.80E-01	7.81E+01	7.81E-01	20
200	2.37E-01	1.25E+02	6.26E-01	50
400	1.77E-01	1.67E+02	4.19E-01	50

The evolution of speedup and efficiency as function of the number of processors for all computational grids used in the current work are presented in Figs. 8 and 9. The code presents a good scalability, with an efficiency bigger than 75%, for grids which have more than 50 million points. Mesh E presented an efficiency of $\approx 100\%$ and speedup of 400 when running on 400 processors. Such performance is equivalent to the theoretical speedup. One can notice a super linear scalability for the cases which the speedup reference is the sequential computation and also for mesh I. The first can be explained by the fact that there is not a serial version of the solver. There is only a parallel version which can run simulations using a single computational core. Moreover, cache memory can be the bottleneck of a simulation using a given mesh and a given number of processors.⁴⁵ Such limitation can explain the super linear speedup of mesh I. The bottleneck can deteriorate the performance of the solver. When the number of processors is increased and mesh size conserved, the cache memory can become no longer a limitation. This effect can generate super-scalability which can be interpreted as computational efficiency greater than 100%.

Table 6. Computational performance of Mesh B.

No. Proc.	Av. CPU time	Speedup	Efficiency	No. Azim. Part.
1	5.78E+01	1.00E+00	1.00E+02	1
2	2.60E+01	2.23E+00	1.11E+02	2
5	7.56E+00	7.65E+00	1.53E+02	1
10	4.38E+00	1.32E+01	1.32E+02	2
20	3.09E+00	1.87E+01	9.36E+01	4
40	1.61E+00	3.59E+01	8.98E+01	8
80	8.43E-01	6.86E+01	8.58E+01	10
100	7.25E-01	7.98E+01	7.98E+01	25
200	3.92E-01	1.48E+02	7.38E+01	25
400	2.60E-01	2.23E+02	5.57E+01	25

Table 7. Computational performance of Mesh C.

No. Proc.	Av. CPU time	Speedup	Efficiency	No. Azim. Part.
1	1.18E+02	1.00E+00	1.00E+02	1
2	5.18E+01	2.28E+00	1.14E+02	1
5	1.68E+01	7.03E+00	1.41E+02	1
10	9.15E+00	1.29E+01	1.29E+02	2
20	6.31E+00	1.87E+01	9.35E+01	4
40	3.27E+00	3.61E+01	9.03E+01	8
80	1.77E+00	6.66E+01	8.33E+01	10
100	1.47E+00	8.05E+01	8.05E+01	20
200	7.89E-01	1.50E+02	7.48E+01	25
400	5.07E-01	2.33E+02	5.82E+01	50

Table 8. Computational performance of Mesh D.

No. Proc.	Av. CPU time	Speedup	Efficiency	No. Azim. Part.
1	2.67E+02	1.00E+00	1.00E+02	1
2	1.04E+02	2.56E+00	1.28E+02	1
5	3.28E+01	8.14E+00	1.63E+02	1
10	1.74E+01	1.54E+01	1.54E+02	2
20	1.21E+01	2.20E+01	1.10E+02	4
40	6.31E+00	4.23E+01	1.06E+02	8
80	3.27E+00	8.17E+01	1.02E+02	8
100	2.73E+00	9.79E+01	9.79E+01	20
200	1.49E+00	1.78E+02	8.92E+01	20
400	8.93E-01	2.99E+02	7.47E+01	25

Table 9. Computational performance of Mesh E.

No. Proc.	Av. CPU time	Speedup	Efficiency	No. Azim. Part.
1	7.02E+02	1.00E+00	1.00E+02	1
2	2.18E+02	3.22E+00	1.61E+02	1
5	7.33E+01	9.58E+00	1.92E+02	1
10	3.68E+01	1.91E+01	1.91E+02	2
20	2.85E+01	2.46E+01	1.23E+02	2
40	1.27E+01	5.53E+01	1.38E+02	8
80	6.67E+00	1.05E+02	1.32E+02	2
100	5.54E+00	1.27E+02	1.27E+02	20
200	3.02E+00	2.33E+02	1.16E+02	20
400	1.70E+00	4.14E+02	1.03E+02	16

Table 10. Computational performance of Mesh F.

No. Proc.	Av. CPU time	Speedup	Efficiency	No. Azim. Part.
40	2.47E+01	4.00E+01	1.00E+02	4
80	1.44E+01	6.87E+01	8.58E+01	8
100	1.04E+01	9.54E+01	9.54E+01	10
200	5.47E+00	1.81E+02	9.04E+01	8
400	3.12E+00	3.17E+02	7.92E+01	8

Table 11. Computational performance of Mesh G.

No. Proc.	Av. CPU time	Speedup	Efficiency	No. Azim. Part.
80	2.61E+01	8.00E+01	1.00E+02	8
100	2.17E+01	9.63E+01	9.63E+01	10
200	1.17E+01	1.78E+02	8.92E+01	8
400	6.76E+00	3.09E+02	7.72E+01	20

Table 12. Computational performance of Mesh H.

No. Proc.	Av. CPU time	Speedup	Efficiency	No. Azim. Part.
200	2.13E+01	2.00E+02	1.00E+02	8
400	1.13E+01	3.75E+02	9.37E+01	16

Table 13. Computational performance of Mesh I.

No. Proc.	Av. CPU time	Speedup	Efficiency	No. Azim. Part.
200	4.09E+01	2.00E+02	1.00E+02	4
400	1.52E+01	5.39E+02	1.35E+02	16

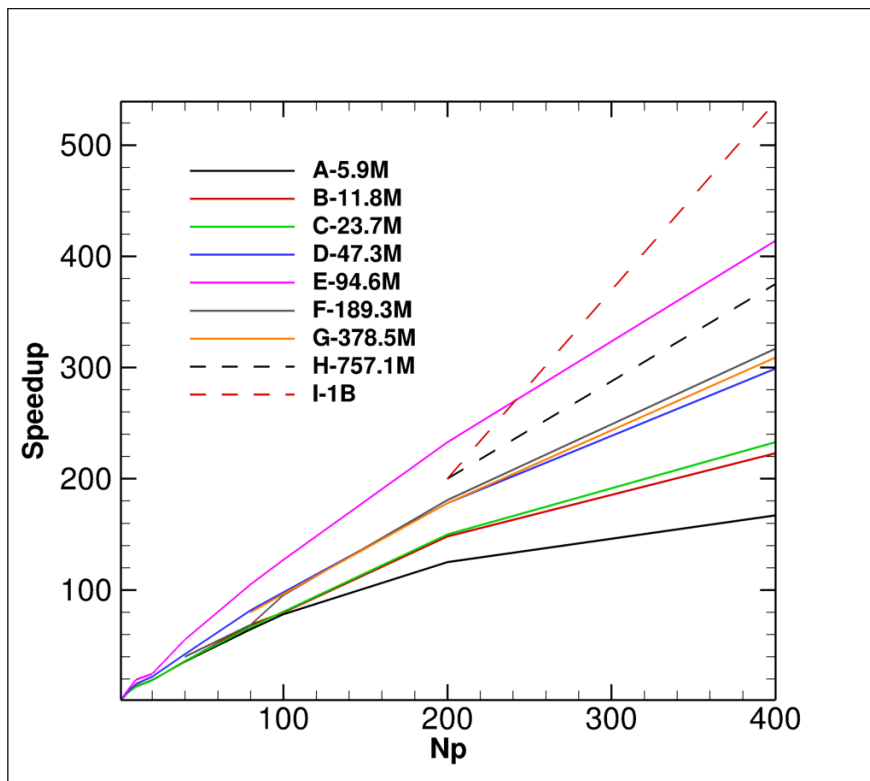


Figure 8. Speedup curve of the LES solver for different mesh sizes.

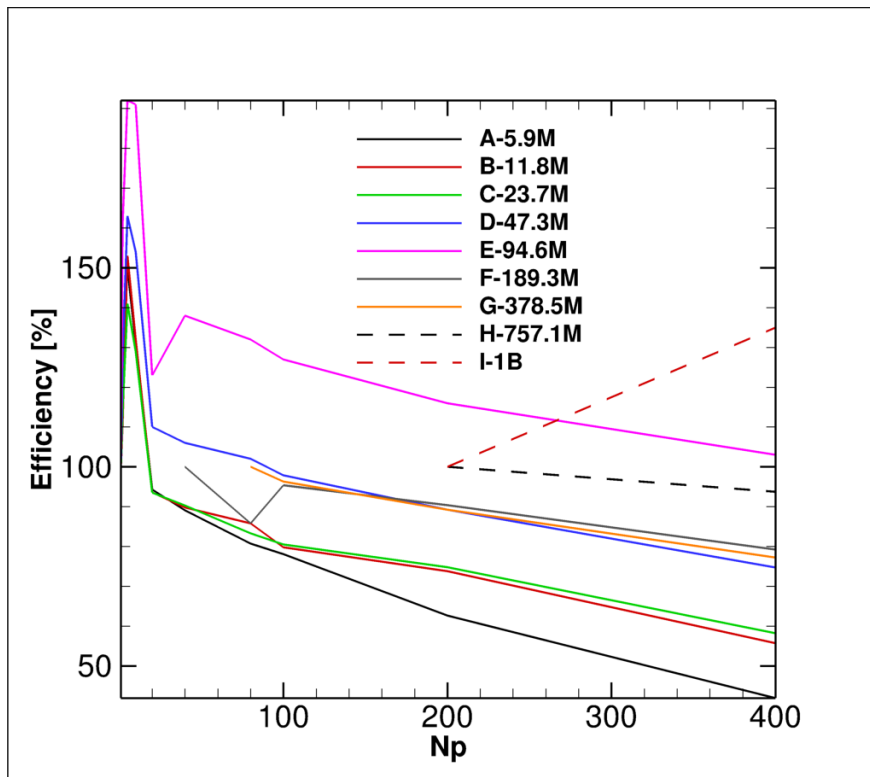


Figure 9. Parallel efficiency of the LES solver for different mesh sizes.

Increasing the size of a computational problem can generate a better scalability study. The time spent with computation becomes more significant when compared to the time spent with communication with the growth of a problem. One can notice such effect for meshes A, B, C, D and E. The speedup and the efficiency increase with with the growth of the mesh size. However, such scalability improvement does not happen from mesh E to meshes F, G, H and I. This behavior is originated because the reference used to calculate speedup and efficiency is not the same for all grid configurations. The studies performed using meshes F, G, H and I does not use the serial computation as a reference, which is not the case for the scalability studies performed in the current paper using mesh A, B, C, D and E.

IX. Concluding Remarks

The current work is a computational performance study of a large eddy simulation solver for supersonic jet flow configurations. Nine strong scalability studies are performed using meshes whose size grows from approximately 5.9 million points to approximately 1.0 billion points. Different partitioning configurations are used to evaluate its effects on the computational performance of the solver. Simulations are run on one processor up to 400 computational cores. The speedup and the computational efficiency are calculated for every study performed in the present article.

The filtered compressible large eddy simulation formulation is written using a finite-difference centered second-order spatial discretization with the explicit addition of artificial dissipation. The time integration is performed using a five-steps second order Runge-Kutta scheme. Three subgrid scale models are implemented into the solver. Message passing interface protocols are used in order to perform the computation in parallel. The code presents parallel-IO features. Each MPI partition reads its portion of the mesh. A mesh generator is created in order to provide balanced CGNS mesh partitions. The solver creates two layers of ghost points in the axial and in azimuthal direction for each partition in order to exchange data with neighbor zones. Communication between partitions are performed using non blocking data exchange towards the best computational performance.

The code presented a good scalability for the calculations run in the current paper. The averaged CPU time per iteration decays with the increase of number of processors in parallel for all computation performed by the large eddy simulation solver evaluated in the present work. Meshes with more than 50 million points indicated an efficiency greater than 75%. The problem with approximately 100 million points presented speedup of 400 and efficiency of 100% when running on 400 computational cores in parallel. Such performance is equivalent to theoretical behavior in parallel. It is important to remark the ability of the parallel solver to treat very dense meshes as the one tested in the present paper with approximately 1.0 billion points. Large eddy simulation demand very refined grids in order to have a well representation of the physical problem of interest. Therefore, it is important to perform simulations of such configuration with a good computation efficiency. One can notice the presence of super-linear speedup in the current study. Such behavior can be explained by cache limitations when running simulations with low amount of computational resources. Moreover, there is no serial version of the code. The sequential study is a parallel version running on one single processor.

Acknowledgments

The authors gratefully acknowledge the partial support for this research provided by Conselho Nacional de Desenvolvimento Científico e Tecnológico, CNPq, under the Research Grants No. 309985/2013-7, No. 400844/2014-1, No. 443839/2014-0 and No. 150551/2017-1. The authors are also indebted to the partial financial support received from Fundação de Amparo à Pesquisa do Estado de São Paulo, FAPESP, under the Research Grants No. 2013/07375-0 and No. 2013/21535-0.

References

- ¹Junqueira-Junior, C. A., *Development of a Parallel Solver for Large Eddy Simulation of Supersonic Jet Flow*, Ph.D. thesis, Instituto Tecnológico de Aeronáutica, São José dos Campos, SP, Brazil, 2016.
- ²Junqueira-Junior, C., Yamouni, S., ao Luiz F. Azevedo, J., and Wolf, W. R., “Influence of Different Subgrid Scale Models in LES of Supersonic Jet Flows,” AIAA Paper No. 2016-4093, *46th AIAA Fluid Dynamics Conference, AIAA Aviation Forum*, Washington, D.C., Jun. 2016.
- ³Wolf, W. R., Azevedo, J. L. F., and Lele, S. K., “Convective Effects and the Role of Quadrupole Sources for Aerofoil Aeroacoustics,” *Journal of Fluid Mechanics*, Vol. 708, 2012, pp. 502–538.
- ⁴Vreman, A. W., *Direct and Large-Eddy Simulation of the Compressible Turbulent Mixing Layer*, Ph.D. thesis, Universiteit Twente, 1995.
- ⁵Mendez, S., Shoeybi, M., Sharma, A., Ham, F. E., Lele, S. K., and Moin, P., “Large-Eddy Simulations of Perfectly-Expanded Supersonic Jets: Quality Assessment and Validation,” AIAA Paper No. 2010-0271, January 2010.
- ⁶Bridges, J. and Wernet, M. P., “Turbulence Associated with Broadband Shock Noise in Hot Jets,” *AIAA paper*, Vol. 2834, 2008, pp. 2008.
- ⁷Folk, M., Cheng, A., and Yates, K., “HDF5: A File Format and I/O Library for High Performance Computing Applications,” *Proceedings of Supercomputing*, Vol. 99, 1999, pp. 5–33.
- ⁸Folk, M., Heber, G., Koziol, Q., Pourmal, E., and Robinson, D., “An Overview of the HDF5 Technology Suite and its Applications,” *Proceedings of the EDBT/ICDT 2011 Workshop on Array Databases*, ACM, 2011, pp. 36–47.
- ⁹Poirier, D. and Enomoto, F. Y., “The CGNS System,” AIAA Paper No. 98-3007, *Proceedings of 29th AIAA Fluid Dynamics Conference*, Albuquerque, NM, June 1998.
- ¹⁰Poirier, D. M. A., Bush, R. H., Cosner, R. R., Rumsey, C. L., and McCarthy, D. R., “Advances in the CGNS Database Standard for Aerodynamics and CFD,” AIAA Paper No. 2000-0681, *38th AIAA Aerospace Sciences Meeting & Exhibit*, Reno, NV, Jan. 2000.
- ¹¹Legensky, S. M., Edwards, D. E., Bush, R. H., and Poirier, D., “CFD General Notation System (CGNS) - Status and Future Directions,” AIAA Paper No. 2002-0752, *Proceedings of 40th AIAA Aerospace Sciences Meeting & Exhibit*, Reno, NV, Jan. 2002.
- ¹²Dongarra, J. J., Otto, S. W., Snir, M., and Walker, D., “An Introduction to the MPI Standard,” Tech. rep., Knoxville, TN, USA, 1995.
- ¹³Sagaut, P., *Large Eddy Simulation for Incompressible Flows*, Springer, 2002.
- ¹⁴Smagorinsky, J., “General Circulation Experiments with the Primitive Equations: I. The Basic Experiment,” *Monthly Weather Review*, Vol. 91, No. 3, March 1963, pp. 99–164.
- ¹⁵Lilly, D. K., “The Representation of Small-Scale Turbulence in Numerical Simulation Experiments,” IBM Form No. 320-1951, *Proceedings of the IBM Scientific Computing Symposium on Environmental Sciences*, Yorktown Heights, N.Y., 1967, pp. 195–210.
- ¹⁶Garnier, E., Adams, N., and Sagaut, P., *Large Eddy Simulation for Compressible Flows*, Springer, 2009.
- ¹⁷Vreman, A. W., “An Eddy-Viscosity Subgrid-Scale Model for Turbulent Shear Flow: Algebraic Theory and Applications,” *Physics of Fluids*, Vol. 16, No. 10, October 2004.
- ¹⁸Lilly, D. K., “On the Computational Stability of Numerical Solutions of Time-Dependent Non-Linear Geophysical Fluid Dynamics Problems,” *Monthly Weather Review*, Vol. 93, No. 1, January 1965, pp. 11–25.
- ¹⁹Deardorff, J. W., “A Numerical Study of Three-Dimensional Turbulent Channel Flow at Large Reynolds Numbers,” *Journal of Fluid Mechanics*, Vol. 41, part 2, 1970, pp. 453–480.
- ²⁰Leonard, A., “Energy Cascade in Large Eddy Simulations of Turbulent Fluid Flows,” *Adv. Geophys.*, Vol. A18, 1974, pp. 237–48.
- ²¹Clark, R. A., Ferziger, J. Z., and Reynolds, W. C., “Evaluation of Subgrid-Scale Models Using an Accurately Simulated Turbulent Flow,” *Journal of Fluid Mechanics*, Vol. 91, 1979, pp. 1–16.
- ²²Vreman, B., Geurts, B., and Kuerten, H., “Large-Eddy Simulation of the Turbulent Mixing Layer Using the Clark Model,” *Theoretical Computational Fluid Dynamics*, Vol. 8, No. 4, 1996, pp. 309–324.
- ²³Germano, M., “Averaging Invariance of the Turbulent Equations and Similar Subgrid Scale Modeling,” *Center for Turbulence Research Manuscript 116*, Stanford University and NASA - Ames Research Center, 1990.
- ²⁴Moin, P., Squires, K., Cabot, W., and Lee, S., “A Dynamic Subgrid-Scale Model for Compressible Turbulence and Scalar Transport,” *Physics of Fluids A: Fluid Dynamics (1989-1993)*, Vol. 3, No. 11, 1991, pp. 2746–2757.
- ²⁵Yoshizawa, A., “Statistical Theory for Compressible Turbulent Shear Flows, with the Application to Subgrid Modeling,” *Physics of Fluids*, Vol. 29, No. 7, July 1986.
- ²⁶Bigarella, E. D. V., *Three-Dimensional Turbulent Flow Over Aerospace Configurations*, M.Sc. Thesis, Instituto Tecnológico de Aeronáutica, São José dos Campos, SP, Brasil, 2002.
- ²⁷Turkel, E. and Vatsa, V. N., “Effect of Artificial Viscosity on Three-Dimensional Flow Solutions,” *AIAA Journal*, Vol. 32, No. 1, 1994, pp. 39–45.
- ²⁸Jameson, A. and Mavriplis, D., “Finite Volume Solution of the Two-Dimensional Euler Equations on a Regular Triangular Mesh,” *AIAA Journal*, Vol. 24, No. 4, Apr. 1986, pp. 611–618.
- ²⁹Jameson, A., Schmidt, W., and Turkel, E., “Numerical Solutions of the Euler Equations by Finite Volume Methods Using Runge-Kutta Time-Stepping Schemes,” AIAA Paper 81-1259, *Proceedings of the AIAA 14th Fluid and Plasma Dynamic Conference*, Palo Alto, California, USA, June 1981.
- ³⁰Long, L. N., Khan, M., and Sharp, H. T., “A Massively Parallel Three-Dimensional Euler/Navier-Stokes Method,” *AIAA Journal*, Vol. 29, No. 5, 1991, pp. 657–666.
- ³¹Bentley, J. L., “Multidimensional Binary Search Trees Used for Associative Searching,” *Communications of the ACM*, Vol. 18, No. 9, 9 1975, pp. 509–517.

- ³²Bentley, J., “Multidimensional Binary Search Trees in Database Applications,” *IEEE Transactions on Software Engineering*, Vol. SE-5, No. 4, 1979, pp. 0–340.
- ³³Germano, M., Piomelli, U., Moin, P., and Cabot, W. H., “A Dynamic Subgridscale Eddy Viscosity Model,” *Physics of Fluids A: Fluid Dynamics*, Vol. 3, No. 7, July 1991.
- ³⁴Balaji, P. and Kimpe, D., “On the Reproducibility of MPI Reduction Operations,” *2013 IEEE 10th International Conference on High Performance Computing and Communications & IEEE International Conference on Embedded and Ubiquitous Computing (HPCC_EUC)*, IEEE, 2013, pp. 407–414.
- ³⁵Arteaga, A., Fuhrer, O., and Hoefer, T., “Designing a Bit-Reproducible Portable High-Performance Applications,” *Parallel and Distributed Processing Symposium, 2014 IEEE 28th International*, Phoenix, AZ, USA, May 2014, pp. 1235–1244.
- ³⁶CEPID-CeMEAI, “Centro de Ciências Aplicadas a Indústria. <http://www.cemeai.icmc.usp.br/>,” .
- ³⁷Lustre [®], “<http://www.lustre.org/>,” .
- ³⁸RedHat, “<http://www.redhat.com/>,” .
- ³⁹Altair - PBS Works[™], “<http://www.pbsworks.com/>,” .
- ⁴⁰Ertel, W., “On the Definition of Speedup,” *PARLE’94 Parallel Architectures and Languages Europe*, Springer, Berlin, 1994, pp. 289–300.
- ⁴¹Gustafson, J. L., “Reevaluating Amdahl’s Law,” *Communications of the ACM*, Vol. 31, No. 5, 1988, pp. 532–533.
- ⁴²Sun, X.-H. and Chen, Y., “Reevaluating Amdahl’s Law in Multicore Era,” *J. Parallel Distrib. Comput.*, Vol. 70, No. 2, Feb. 2010, pp. 183–188.
- ⁴³Amdahl, G. M., “Validity of the Single Processor Approach to Achieving Large Scale Computing Capabilities,” *AFIPS Conference Proceedings*, Vol. 30, ACM, Atlantic City, N.J., USA, Apr. 1967, pp. 483–485.
- ⁴⁴Junqueira-Junior, C., Yamouni, S., Azevedo, J. L. F., and Wolf, W. R., “Large Eddy Simulations of Supersonic Jet Flows for Aeroacoustic Applications,” AIAA Paper No. 2015-3306, *Proceedings of the 33rd AIAA Applied Aerodynamics Conference*, Dallas, TX, June 2015.
- ⁴⁵Benzi, J. and Damodaran, M., “Parallel Three Dimensional Direct Simulation Monte Carlo for Simulating Micro Flows,” *Parallel Computational Fluid Dynamics 2007*, Springer, 2009, pp. 91–98.